ACS OMEGA

Open Access

http://pubs.acs.org/journal/acsodf

Article

Stereoselective Biosynthesis of Bichiral Amino Alcohols from Diketone via Difunctionalization

Tianfu Wu, Wei Song, Jing Wu, Jian Wen, Wanqing Wei,* and Liming Liu*

Cite This: *ACS Omega* 2025, 10, 23409−23420

Read Online

ACCESS | Metrics & More | Article Recommendations | Supporting Information

ABSTRACT: Chiral amino alcohols are vital in many biologically active molecules and natural products and are crucial building blocks for the pharmaceutical industry. However, the chemosynthesis of chiral amino alcohols, particularly bichiral amino alcohols, faces challenges related to chemoselectivity and enantioselectivity. Here, a dual-enzyme cascade pathway for the synthesis of bichiral amino alcohols through difunctionalization, exhibiting both high chemo- and stereoselectivity, was proposed for the first time. Among them, NADPH-dependent *meso*-diaminopyrimidate dehydrogenase from *Proteus vulgaris* (*Pv*DAPDH) exhibited (*R*)-selective reductive amination activity, converting ketones into chiral amines; natural glucose dehydrogenase from *Bacillus megaterium* (*Bm*GDH) not only facilitated NADPH regeneration but also catalyzed the reductive hydroxylation of ketones to chiral alcohols. Second, the rational design of the rate-limiting enzyme *Pv*DAPDH generated the mutant M4 with increased specific activity and catalytic efficiency (k_{cat}/K_m) for **16a** up to 3.2- and 10.3-fold, respectively, compared to the wild type. Additionally, the yield of mutant M4 for **1a**−**16a** increased by 1.1- to 37-fold compared to the wild type. Finally, two high-value bichiral amino alcohols (**14b** and **16b**) were asymmetrically synthesized from the corresponding bietone via a one-pot dual-enzyme cascade, exhibiting excellent stereoselectivity (dr ≥ 98:2). These findings provide a potential biosynthetic pathway for the green synthesis of bichiral amino alcohols and complement existing synthetic methods.

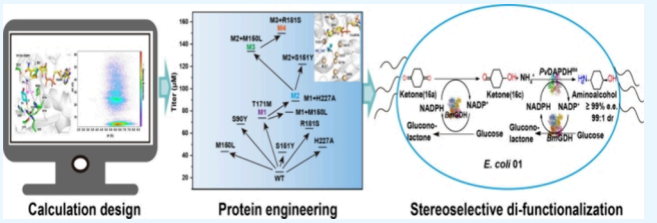

INTRODUCTION

Chiral amino alcohols are ubiquitous structural motifs present in many biologically active molecules and natural products, as well as being crucial intermediates in pharmaceutical synthesis, for example, antibacterial drugs, anticancer drugs, anti-HIV drugs, and drugs used to treat Alzheimer's disease (Scheme 1a).[1−5]

Various chemosynthetic methods have been developed, including Sharpless asymmetric amino hydroxylation of olefins,[6,7] reduction of amino/hydroxy ketones,[8−10] cross-coupling of imines with carbonyl compounds,[11] and asymmetric ring opening of epoxides (Scheme 1b).[12,13] However, the chemoselectivity resulting from the construction of two polar bonds in the synthesis of amino alcohols required additional protection and deprotection steps. Although the transformations involving radical intermediates were compatible with common functional groups,[14] achieving enantioselectivity remained a challenge due to the lack of suitable radical acceptors and reliable stereocontrol.[15,16]

Biosynthesis is an alternative due to its high selectivity and mild conditions for the synthesis of chiral amino alcohols (Scheme 1c). The enzymes that catalyzed the asymmetric monofunctionalization of monoketones included ω-transaminases (ω-TAs),[17,18] imine reductases (IREDs) or amine dehydrogenation enzymes (AmDHs) for the asymmetric reductive amination of hydroxyl ketones,[19−24] as well as ketone reductases (KREDs) or carbonyl reductases for the asymmetric reductive hydroxylation of amino ketones.[25,26] In addition, engineered cytochrome *c* had been reported to difunctionalize olefin into monochiral amino alcohols.[27] 4-Aminocyclohexanol was synthesized using aminotransferase and ketone reductase in one pot, achieving a titer of 40 mM with excellent cis-selectivity (cis/trans = 99:1) but poor trans-selectivity (cis/trans = 3:7).[28] An engineered AmDH catalyzed the asymmetric reductive amination of α-hydroxy ketones to produce (*S*)-chiral amino alcohols, with remarkable conversion rates and enantiomeric excess >99%.[19] A mutant mh13 capable of synthesizing (*R*)-chiral amino alcohols was obtained by directed evolution of *Gs*AmDH from *Geobacillus stearothermophilus* with excellent enantioselectivity (enantiomeric excess (ee) > 99%) but narrow substrate scope and poor catalytic activity.[22] Furthermore, engineered IREDs synthesized (*R*)-*N*-substituted 1,2-amino alcohols with excellent stereoselectivity (ee > 99%), but primary amino alcohols were not being synthesized.[23] Native amine dehydrogenase and *Asp*RedAm can catalyze the reductive amination of various cyclic ketones

Received: February 27, 2025
Revised: April 16, 2025
Accepted: April 24, 2025
Published: May 27, 2025

Scheme 1. Importance of Chiral Amino Alcohols and Synthetic Approaches[a]

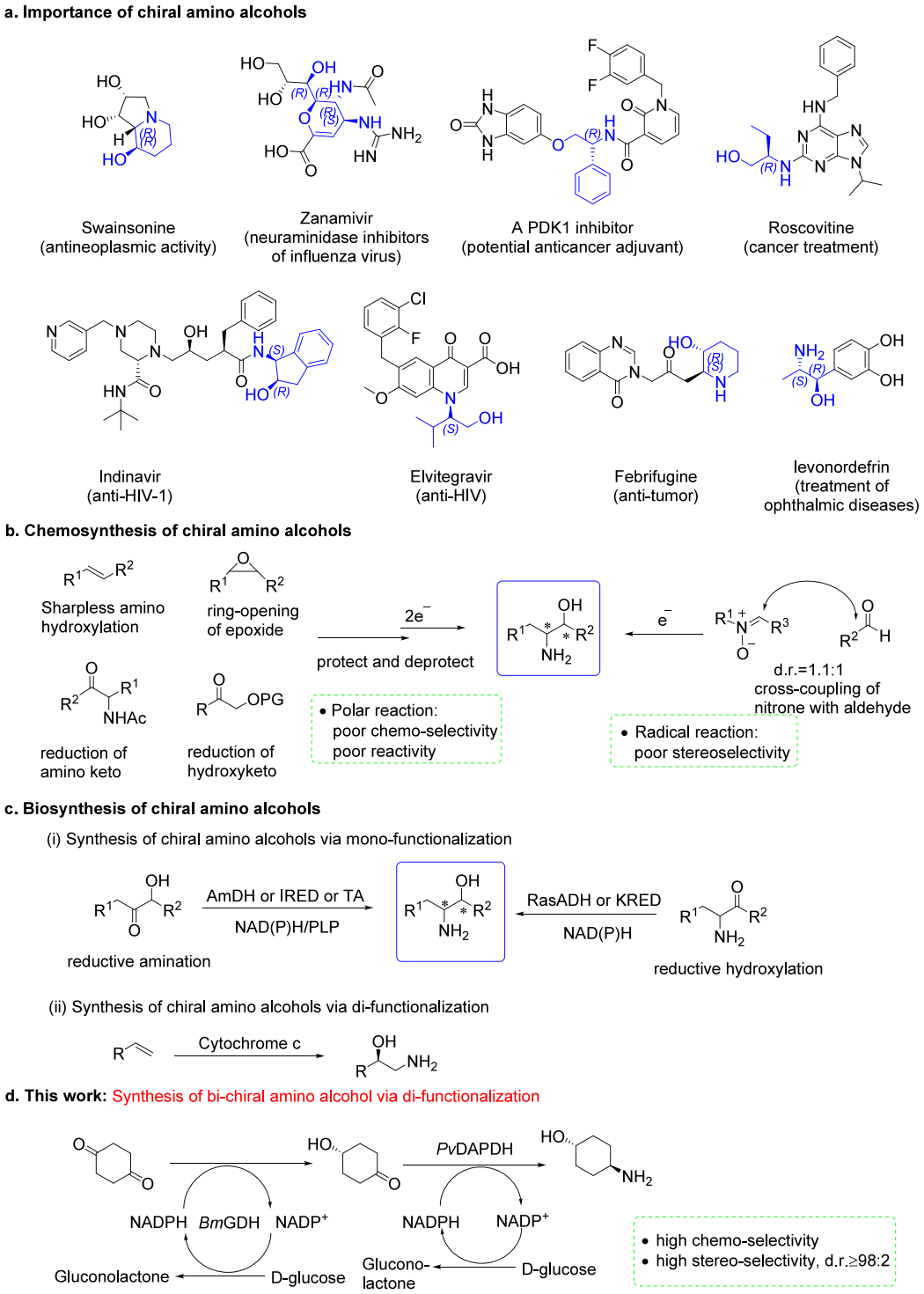

[a](a) Importance of chiral amino alcohols, (b) chemosynthesis of chiral amino alcohols, (c) biosynthesis of chiral amino alcohols, and (d) stereoselective sequential synthesis of bichiral amino alcohols using *Pv*DAPDH and bifunctional *Bm*GDH.

to synthesize chiral amines and their derivatives but with no catalytic activity against hydroxyketone substrates.[24,29] The *Ras*ADH/photoredox catalyzed the radical decarboxylative coupling reaction of amino acids and carbonyls to synthesize chiral 1,2-amino alcohols with high enantioselectivity (ee ≥ 92% *S*), but harsh reaction conditions limit its wide application.[26] Therefore, the installation of multiple functional groups and the construction of two or more stereocenters in one building block need to be further solved.

In this study, we reported an effective solution to synthesize high-value bichiral amino alcohols with (*R*)-enantiomers through a dual-enzyme cascade system via difunctionalization of biketone (Scheme 1d). *Pv*DAPDH exhibited extended (*R*)-selective reductive amination activity from ketone acid to general ketone for the first time, with excellent stereoselectivity

https://doi.org/10.1021/acsomega.5c01864
ACS Omega 2025, 10, 23409−23420

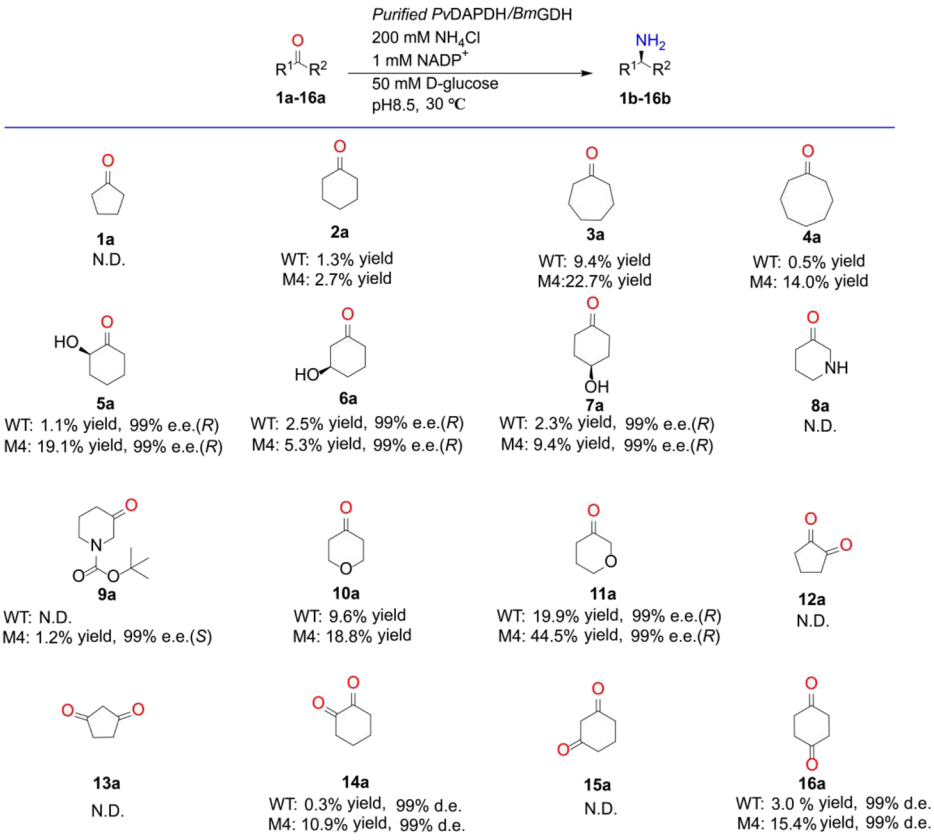

Figure 1. The catalytic performance of the *Bm*GDH/*Pv*DAPDH cascade system. The products were determined via chiral high-performance liquid chromatography (HPLC) and gas chromatography (GC) using 20 mM ketone substrate, 1 mM $NADP^+$, 200 mM NH_4Cl, 50 mM D-glucose, and purified *Pv*DAPDH/*Bm*GDH in a Tris-HCl buffer (100 mM, pH 8.5) at 30 °C. All experiments were conducted in triplicate. N.D.: not detected.

(ee > 99%). Natural *Bm*GDH had not only the function of cofactor regeneration but also the function of reductively hydroxylated ketones. Second, rational design guided by the catalytic mechanism mutant *Pv*DAPDH^{M4} obtained increased catalytic activity toward ketone substrates. Finally, two high-value-added bichiral amino alcohols were asymmetrically synthesized via the one-pot dual-enzyme cascade using inexpensive diketone substrates. These findings may provide a potential biosynthetic pathway for the green production of high-value bichiral amino alcohols.

RESULTS AND DISCUSSION

Discovery of Bichiral Amino Alcohol Biosynthesis. Our previous study found that the rational design of *Pv*DAPDH can extend the substrate from aliphatic ketone acids to aromatic ketone acids, thereby reducing amination to generate the corresponding D-amino acids. To further expand the substrate scope of *Pv*DAPDH, we investigated the potential for catalyzing the reductive amination of generalized ketones to produce *R*-chiral amines. The reductive amination activity of aromatic, aliphatic, and alicyclic ketones was evaluated utilizing a purified dual-enzyme cascade system comprising *Pv*DAPDH and glucose dehydrogenase from *Bacillus megaterium* (*Bm*GDH), which is frequently employed for NADPH regeneration. Fortunately, some alicyclic ketones (**2a**−**7a**, **10a**−**11a**, **14a**, and **16a**) were highly stereospecifically reduced to the corresponding *R*-chiral amines (ee ≥ 99%) but with lower activity (Figure 1 and Figure S1). Among them, **11a** showed the highest activity, with a conversion rate of 19.9%. To our surprise, alicyclic monoketones (**2a**, **5a**, **7a**, **8a**, and **10a**) were mainly asymmetrically reduced to chiral alcohols (Figure S2). More interestingly, the inexpensive and readily accessible alicyclic diketones **14a** and **16a** were successfully asymmetrically reduced to generate high-value dichiral amino alcohols **14b** and **16b** (Figure 1).

To investigate how the dicarbonyl group in **16a** is asymmetrically reduced to produce dichiral amino alcohol by the dual-enzyme cascade system, we conducted detailed control experiments. Using **16a** as the substrate, 3.1% chiral amino alcohol **16b** was detected only in the presence of both *Pv*DAPDH and *Bm*GDH. (Figure 2 and Table S2, entry 1). Using **16a** as substrate, when only under the catalysis of *Bm*GDH, the products **16c** and **16d** of asymmetric reductive hydroxylation were detected (Figure 2 and Table S2, entries 2 and 4). In contrast, when only under the catalysis of *Pv*DAPDH, no product of asymmetric reductive amination or hydroxylation was detected with **16a** as the substrate (Figure 2b and Table S2, entry 3). However, the asymmetric reductive amination product **16b** was detected with **16c** as a substrate (Figure 2a and Table S2, entry 5). Together, *Pv*DAPDH exhibits the ability to perform asymmetric reductive amination of ketone carbonyl to produce (*R*)-chiral amines, while *Bm*GDH not only regenerates the NADPH cofactor but also has the function of asymmetric reductive hydroxylation of ketone carbonyl to generate (*R*)-chiral alcohols.

Identification and Optimization of Bichiral Amino Alcohol Biosynthesis. Two possible synthetic pathways from **16a** to **16b** were hypothesized: route A and route B (Figure 3a). To further elucidate the synthetic pathway of **16b**, we

https://doi.org/10.1021/acsomega.5c01864
ACS Omega 2025, 10, 23409−23420

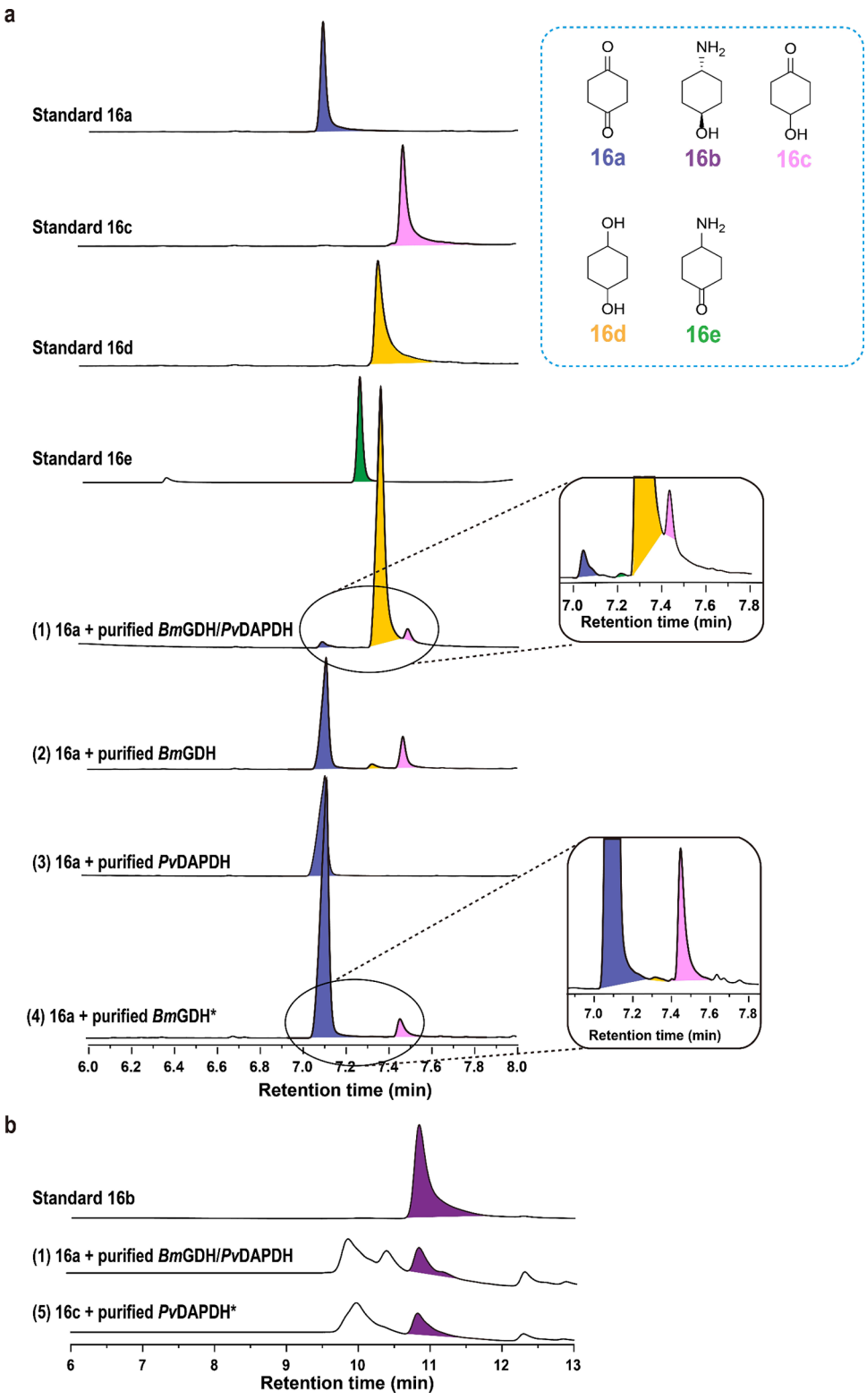

Figure 2. The functional verification of the *Bm*GDH/*Pv*DAPDH cascade system. (a) Chiral HPLC was used for production identification. (b) GC was used for production identification. The products were determined via chiral HPLC and GC using 10 mM **16a** or **16c**, 1 mM $NADP^+$, 100 mM NH_4Cl, 50 mM D-glucose, and purified *Bm*GDH/*Pv*DAPDH in a Tris-HCl buffer (100 mM, pH 8.5) at 30 °C. *NADPH was added to the reaction system. See Table S2 for the details.

analyzed the reaction process curve (Figure 3b). As substrate **16a** was consumed, intermediate **16c** gradually accumulated. Subsequently, intermediate **16c** was partially converted into product **16b** and byproduct **16d**, and a small amount of intermediate **16e** was also generated. In addition, no 1,4-cyclohexanediamine products were detected during the reaction (Figure 3b). Therefore, substrate **16a** first underwent reductive hydroxylation by *Bm*GDH to form intermediate **16c** and subsequently underwent asymmetric reductive amination

https://doi.org/10.1021/acsomega.5c01864
ACS Omega 2025, 10, 23409−23420

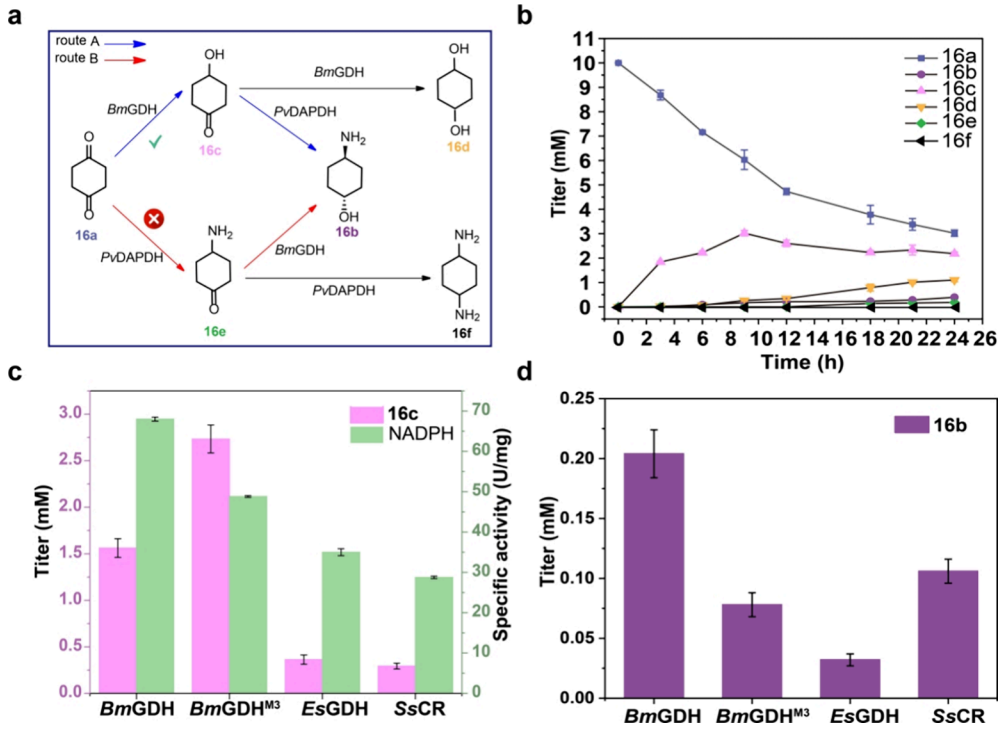

Figure 3. Identification and optimization of the synthetic pathway of **16b**. (a) Identification of the synthetic pathway for **16b**. (b) The reaction process curve of **16b**. The products were determined using 20 mM **16a**, 1 mM $NADP^+$, 200 mM NH_4Cl, and 50 mM D-glucose and purified *Bm*GDH/*Pv*DAPDH in a Tris-HCl buffer (100 mM, pH 8.5) at 30 °C. (c) Optimization of the pathway enzyme. The specific activity was determined using 1 mM $NADP^+$, 50 mM D-glucose, and four purified enzymes in a Tris-HCl buffer (100 mM, pH 8.5) at 30 °C. The titer of the **16c** was determined using 10 mM **16a**, 1 mM $NADP^+$, 50 mM D-glucose, and four purified enzymes in a Tris-HCl buffer (100 mM, pH 8.5) at 30 °C. (d) The activity of **16b** was determined using four purified enzymes and *Pv*DAPDH. The titer of the **16b** was determined using 10 mM **16a**, 1 mM $NADP^+$, 100 mM NH_4Cl, 50 mM D-glucose, four purified enzymes, and *Pv*DAPDH in a Tris-HCl buffer (100 mM, pH 8.5) at 30 °C. All experiments were conducted in triplicate.

Table 1. Kinetic Parameters and Specific Activities of *Bm*GDH, *Pv*DAPDH, and Its Mutant

enzyme	substrate	K_m (mM)[a]	k_{cat} (s^{-1})	k_{cat}/K_m ($mM^{-1}\cdot s^{-1}$)	specific activity (U/mg)
*Bm*GDH	**16a**	50.03 ± 7.70	34.80 ± 0.50	0.70	6.72 ± 0.10
*Pv*DAPDH	**16c**	9.42 ± 3.00	0.24 ± 0.03	0.03 (1)	0.05 ± 0.01 (1)
$PvDAPDH^{M4}$	**16c**	1.47 ± 0.14	0.50 ± 0.01	0.34 (11.3)	0.21 ± 0.02 (4.2)

[a]The kinetic parameters of *Bm*GDH, *Pv*DAPDH, and its mutant were determined in a Tris-HCl buffer (100 mM, pH 8.5) at 30 °C, which contained 200 mM NH_4Cl, 5 mM NADPH with various concentrations of **16a** or **16c** (0−50 mM), and purified enzymes. All experiments were conducted in triplicate. K_m values were obtained by fitting the Michaelis−Menten equation.

by *Pv*DAPDH to produce **16b**, following synthetic route A (Figure 3a).

To optimize the synthesis pathway of **16b**, we screened enzymes for cofactor regeneration and asymmetric reductive hydroxylation. Based on the principle of substrate structure similarity, the reported glucose dehydrogenases (*Bm*GDH, *Bm*GDH-M3, and *Es*GDH) from *Bacillus subtilis* and *Exiguobacterium sibiricum*, as well as the ketone reductase (*Ss*CR) from *Sporobolomyces salmonicolor*, were screened. SDS-PAGE results indicated that all four enzymes exhibited good soluble expression, with *Bm*GDH having the highest protein expression (Figure S3). The capabilities for cofactor regeneration and asymmetric reductive hydroxylation were evaluated by measuring the specific activity of regenerated NADPH and the titer of asymmetrically reduced hydroxylation **16a** to **16c**. The results revealed that *Bm*GDH regenerated NADPH with the highest specific activity, while $BmGDH^{M3}$ catalyzed **16a** to produce **16c** with the highest titer (Figure 3c). Subsequently, the purified dual-enzyme cascade system of the four enzymes mentioned above and *Pv*DAPDH was constructed to determine the production of **16b**. The results indicated that the system containing *Bm*GDH achieved the highest titer of **16b**, which was 0.2 ± 0.02 mM (Figure 3d). Therefore, *Bm*GDH was selected for a subsequent study.

Mechanism Analysis of *Pv*DAPDH. Given that the accumulation of intermediate **16c** and the catalytic efficiency of *Pv*DAPDH for intermediate **16c** are lower than those of *Bm*GDH for substrate **16a**, *Pv*DAPDH is the rate-limiting enzyme in this synthetic pathway (Figure 3b and Table 1). To elucidate the reason for the low catalytic efficiency of *Pv*DAPDH toward intermediate **16c**, we compared the kinetic parameters of *Pv*DAPDH for intermediate **16c** and its natural substrate. The K_m value of *Pv*DAPDH for intermediate **16c** (K_m = 9.42 ± 0.30 mM) was 23 times higher than that of *St*DAPDH for its natural substrate *meso*-DAP[30] (K_m = 0.41 ± 0.07 mM). The k_{cat} value of *Pv*DAPDH for intermediate **16c** (k_{cat} = 0.24 s^{-1}) was approximately 1/169 that of *St*DAPDH for the natural substrate (k_{cat} = 40.47 ± 2.95 s^{-1}). Therefore,

https://doi.org/10.1021/acsomega.5c01864
ACS Omega 2025, 10, 23409−23420

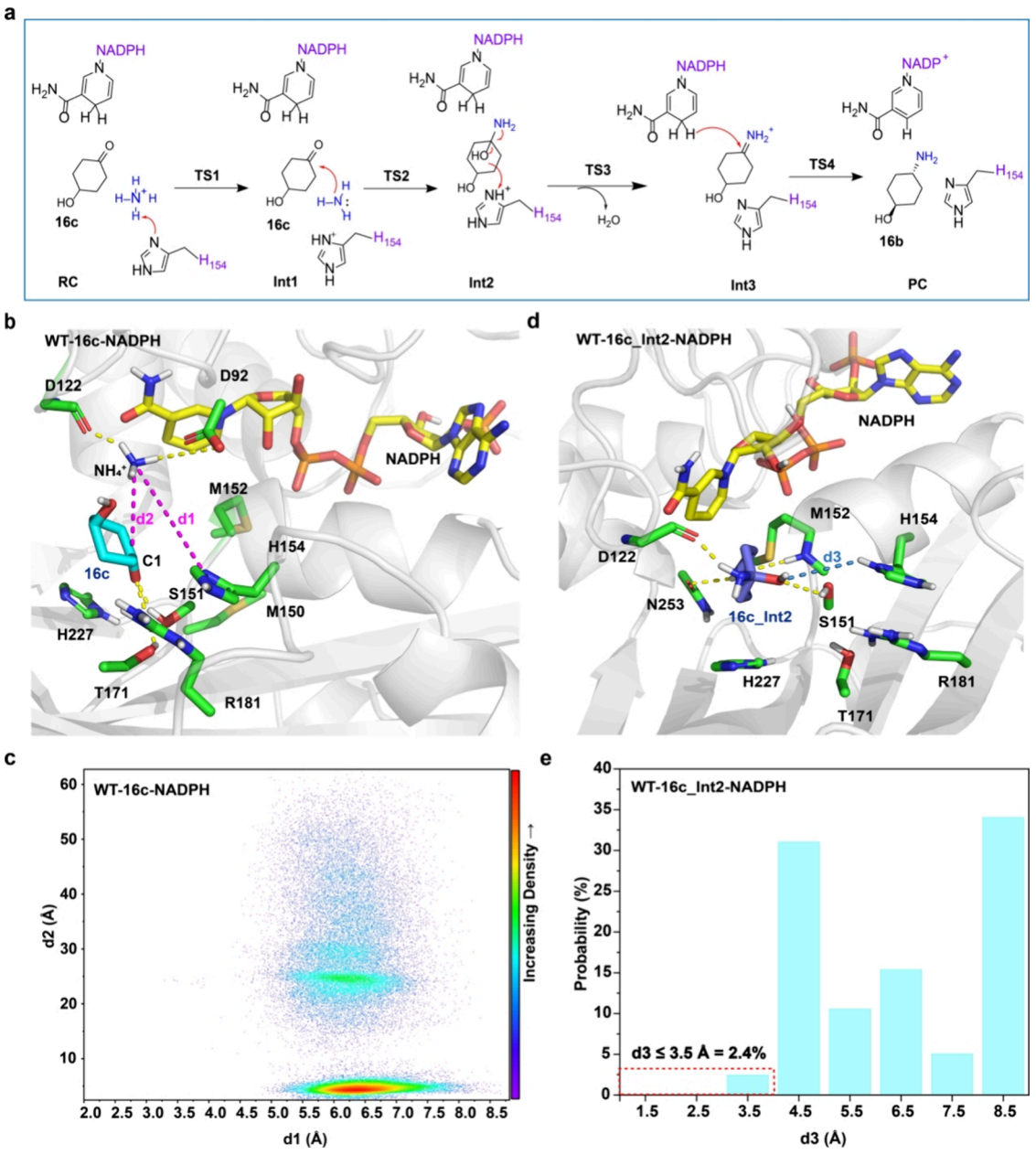

Figure 4. Catalytic mechanism of *Pv*DAPDH. (a) Proposed molecular mechanism of *Pv*DAPDH. (b) The possible binding mode of **16c** in *Pv*DAPDH (**16c** in cyan stick, NH_4^+ in blue stick, and hydrogen bonds in yellow dashed lines). (c) MD plots for the distances of the ammonium ion activation (d1) and the formation of the N−C bond (d2) in *Pv*DAPDH-**16c**-NADPH. (d) Possible binding mode of **16c**_Int2 in *Pv*DAPDH (**16c**_Int2 in purple sticks and hydrogen bonds in yellow dashed lines). (e) MD plots for proton-transfer distance d3 in *Pv*DAPDH-**16c**_int2-NADPH.

the low catalytic efficiency of *Pv*DAPDH for intermediate **16c** is primarily attributed to the low turnover number.

Our previous studies have demonstrated that the reductive amination of *Pv*DAPDH can be divided into four steps: the activation of the ammonium ion (RC → [TS1]), the formation of an alcoholamine intermediate via nucleophilic attack (Int1 → [TS2]), the dehydration of an alcoholamine intermediate to form an iminium ion intermediate (Int2 → [TS3]), and the reduction of an iminium ion intermediate to generate a chiral amine (Int3 → [TS4]). Among these steps, the activation of ammonium ions, the nucleophilic attack, and the dehydration of the alcoholamine intermediate represent high-energy barrier steps.[31] Therefore, we docked **16c** and intermediate **16c**_Int2 into the active center of the *Pv*DAPDH-$NADP^+$ binary complex and performed molecular dynamics (MD) simulations to obtain a dynamically stable ternary complex structure.

For the activation of the ammonium ion and the nucleophilic attack (RC → [TS1] and Int1 → [TS2]) reaction step, a two-dimensional descriptor was employed to characterize the catalytic conformation of **16c** (Figure 4b). The first dimension, distance 1 [d1(N@NH_4^+-NE1@H154)], denotes the distance between the nitrogen atom of NH_4^+ and the NE1 atom on the side chain imidazolium ring of residue H154. This distance was utilized to depict NH_4^+ activation by residue H154. The second dimension, distance 2 [d2(N@NH_4^+-C1@**16c**)], refers to the distance between the nitrogen atom of NH_4^+ and the C1 atom of **16c**. This distance was employed to represent the activated NH_4^+ nucleophilic attack on the C1

https://doi.org/10.1021/acsomega.5c01864
ACS Omega 2025, 10, 23409−23420

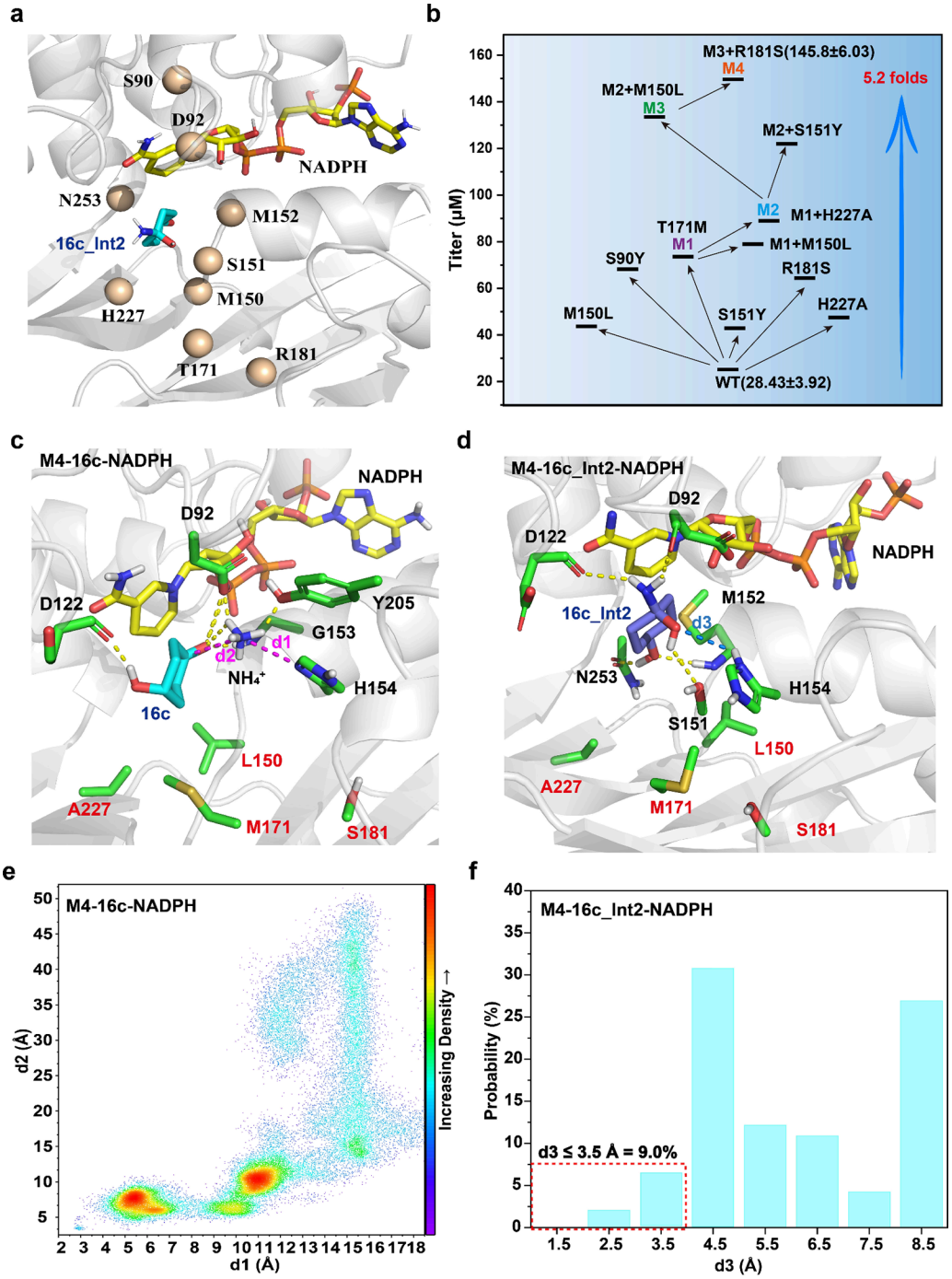

Figure 5. Protein engineering of *Pv*DAPDH. (a) Potential mutation sites (light orange sphere). (b) Mutation process of *Pv*DAPDH. The assay system consisted of 10 mM **16c**, 100 mM NH_4Cl, 2 mM NADPH, and crude enzyme in a Tris-HCl buffer (100 mM, pH 8.5) at 30 °C. All experiments were conducted in triplicate. (c) The possible binding mode of **16c** in mutant M4 (**16c** in cyan stick, NH_4^+ in blue stick, and hydrogen bonds in yellow dashed lines). (d) The possible binding mode of **16c_Int2** in mutant M4 (**16c_Int2** in purple stick and hydrogen bonds in yellow dashed lines). (e) MD plots for the distances of the ammonium ion activation (d1) and the forming of the N−C bond (d2) in M4-**16c**-NADPH. (f) The probability distribution of proton transfer distance d3 between **16c_Int2** and H154 in mutant M4.

atom of **16c**. The catalytic conformation needs to satisfy both d1 ≤ 3.3 and d2 ≤ 3.5 Å. MD simulations revealed that the catalytic conformation ratio of **16c** is extremely low (Figure 4c, 0.01%), suggesting that the probability of activation and nucleophilic attack of ammonium ion is low. The nitrogen atom of the ammonium ion forms hydrogen bonds with the side chain carboxyl oxygen atom of residue D92 and the main chain carbonyl oxygen atom of residue D122, which may result in the ammonium ion being far away from residue H154. The carbonyl oxygen on C1 of **16c** forms hydrogen bonds with the side chain hydroxyl groups of residues S151 and T171. Additionally, the CH-π interaction between the alicyclic ring of **16c** and the imidazole ring of residue H227 may lead to a long distance between the ammonium ion and **16c**. Therefore, altering the charged properties of the residues surrounding the ammonium ion shortens the activation distance of the

https://doi.org/10.1021/acsomega.5c01864
ACS Omega 2025, 10, 23409−23420

ammonium ion. Additionally, strengthening the interaction between **16c** and the surrounding residues could decrease the distance for the amine nucleophilic attack.

For the alcoholamine intermediate dehydration Int2 → [TS3] reaction step, the key distance of the catalytic conformation of **16c**_Int2 is d3 (HD1@H154-O@ **16c**_Int2), denoting the distance between the hydrogen atom HD1 on the side chain imidazole ring of residue H154 and the oxygen atom within the hydroxyl group on **16c**_Int2. This distance represents the proton transfer from residue H154 to **16c**_Int2 (Figure 4d). MD simulations showed that the conformational proportion of d3 ≤ 3.5 Å was only 2.4% (Figure 4e), indicating a low probability of proton transfer. Hydrogen bonds are formed between the amino hydrogen atom on C1 of **16c**_Int2 and the main chain carbonyl oxygen atom of residue D122, as well as between the hydroxyl oxygen atom on C1 of **16c**_Int2 and the side chain hydroxyl hydrogen atom of residue S151. Additionally, the hydroxyl group on C4 of **16c**_Int2 forms hydrogen bonds with the side chain amide oxygen atom of residue N253 and the main chain amino hydrogen atom of residue M152. The aforementioned forces may cause **16c**_Int2 to deviate from the active center. Consequently, by altering the interaction between **16c**_Int2 and the surrounding residues, either **16c**_Int2 is pushed toward residue H154 or the α-helix of residue H154 is brought closer to **16c**_Int2, thereby reducing the distance for proton transfer. Overall, we identified nine nonconserved amino acid residues (S90, D92, M150, S151, M152, T171, R181, H227, and N253) near the ammonium ion, **16c**, and **16c**_Int2 as potential mutation sites.

Protein Engineering of *Pv*DAPDH. Based on the chromogenic principle of 2,4-dinitrophenylhydrazine (DNPs), a strong linear relationship was observed between the absorbance at 520 nm and the concentration of **16c** (R^2 = 0.9974), which was used as a high-throughput screening method (Figure S6). A saturated single mutant library on the nine potential mutation sites was constructed using NNK degenerate codons (Figure 5a and Table S3).

In the first round of mutation, 27 potential positive mutants (Table S5) were obtained through DNPs screening, and 6 beneficial single mutants (S90Y, M150L, S151Y, T171M, R181S, and H227A) were identified by HPLC determination. Among these, the titer of the optimal single mutant T171 M increased by 155.6% compared to the wild type (WT), which was recorded as M1 (Figure 5b and Table S6). In the second round of mutations, M1 was used as a template for iterative combinatorial mutations with the other five beneficial single mutants, resulting in the construction of five double mutants (Figure 5b and Table S6). The results indicated that the positive double mutants were T171M/H227A and T171M/M150L, with the optimal double mutant T171M/H227A showing a 21.5% increase in titer over M1, which was recorded as M2. In the third round of mutations, M2 served as a template for iterative combinatorial mutations with the remaining four beneficial single mutants to construct a four triple mutants' library (Figure 5b and Table S6). The results showed that the positive triple mutants were T171M/H227A/M150L and T171M/H227A/S151Y, and the optimal triple mutant T171M/H227A/M150L was 45.8% higher than M2, denoted as M3. In the fourth round of mutations, M3 was used as a template, and the remaining three beneficial single mutants were iteratively combined to construct three quadruple mutants (Figure 5b and Table S6). The positive quadruple mutants were T171M/H227A/M150L/R181S, and the titer was 13.2% higher than that of M3, which was recorded as M4. In the fifth round of mutation, M4 served as the template for further iterative combinatorial mutations with the remaining two beneficial single mutants, resulting in the construction of two quintuple mutants (Figure 5b and Table S6). However, no positive quintuple mutants were identified. Therefore, mutant M4 was chosen for further study (Figure 5b and Table S6).

To characterize the catalytic performance of mutant M4, we determined the specific activity and kinetic parameters of mutant M4 for **16c**. Compared to that of the WT, the specific activity of mutant M4 for **16c** increased by 3.2 times (Table 1). The K_m value of mutant M4 for **16c** was 5.4 times lower than that of the WT, indicating an enhanced affinity of mutant M4 for **16c**. Additionally, the k_{cat} value of mutant M4 for **16c** improved by 1.1 times, suggesting an increased reaction rate. Consequently, the catalytic efficiency (k_{cat}/K_m) of mutant M4 for **16c** was 10.3 times higher than that of the WT (Table 1).

To elucidate the molecular mechanism underlying the enhanced catalytic activity of mutant M4, we analyzed the proportion of catalytic conformations in three high-energy barrier steps (RC → [TS1], Int1 → [TS2], and Int2 → TS3). **16c** and **16c**_Int2 were docked into the active center of mutant M4, and MD simulations were subsequently performed. The results revealed that the proportion of catalytic conformations (d1 and d2) increased from 0.01% in WT to 0.20% in mutant M4 (Figures 4c and 5e). The T171 M mutation disrupted the hydrogen bond interaction with the carbonyl oxygen at the C1 position of **16c**, leading to an upward deflection of the **16c** conformation. This alteration resulted in the formation of new hydrogen bond interactions with residues D92, D122, G153, and NADPH, thereby reducing the distance for the nucleophilic attack (d2: 4.5 → 3.3 Å; Figures 4b and 5c). Additionally, a new hydrogen bond interaction between the ammonium ion and the phenolic hydroxyl group of residue Y205 draws the ammonium ion closer to residue H154, reducing the activation distance of the ammonium ion (d1: 6.4 → 4.5 Å) (Figures 4b and 5c). Furthermore, the proportion of the catalytic conformation (d3) in mutant M4 increased from 2.4% in the WT to 9.0% (Figures 4d and 5f). The H227A mutation disrupted the CH-π interaction with **16c**_Int2 and established a new hydrogen bond with D92, resulting in an upward shift of **16c**_Int2. Additionally, the R181S mutation may eliminate the electrostatic repulsion between residue H154 and facilitate the free rotation of residue H154 toward **16c**_Int2, thereby shortening the proton transfer distance between **16c**_Int2 and residue H154 (d3: 4.1 → 3.1 Å) (Figures 4d and 5d). These results indicated that mutants M150S, T171M, R181S, and H227A altered the electric field environment within the active site, shortened the proton transfer distance, increased the proportion of the catalytic conformation, and consequently enhanced the catalytic efficiency.

The substrate scope of the mutant M4 was evaluated, and the results indicated that compared with WT, the mutant M4 exhibited better catalytic activity for alicyclic ketones (**1a**−**16a**), including **9a**, which WT could not convert. The yield of mutant M4 to various alicyclic ketones increased by 1.1−37 times, with mutant M4 exhibiting the highest enhancement of 37-fold for **14a**. Unfortunately, no activity was observed for aliphatic and aromatic ketones (Figure 1).

Whole Cell Synthesis of High-Value Bichiral Amino Alcohols. To achieve the biosynthesis of high-value bichiral

https://doi.org/10.1021/acsomega.5c01864
ACS Omega 2025, 10, 23409−23420

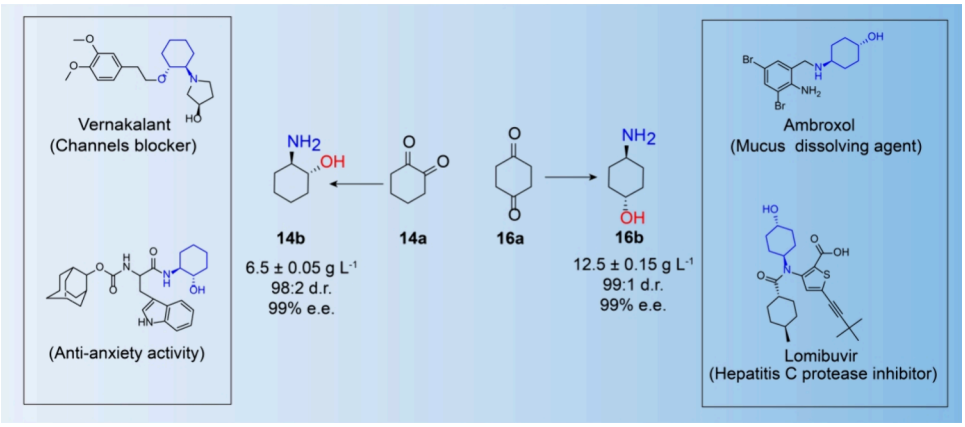

Figure 6. One-pot biosynthesis of high-value bichiral amino alcohols. The transformation reaction system consisted of a 20 mL Tris-HCl buffer (100 mM, pH 8.5) containing 50 g L^{-1} cyclohexanedione substrate, 30 g L^{-1} NH_4Cl, 100 g L^{-1} D-glucose, 1.0 mM $NADP^+$, and whole cell *E. coli* 01 biocatalysts. The products were determined via chiral HPLC after reaction for 30 h at 30 °C. All experiments were conducted in triplicate.

amino alcohols, we inserted the genes encoding *Pv*DAPDH^{M4} and *Bm*GDH into the high-copy plasmid pRSFDuet-1 (Figure S7). This plasmid was then transformed into *E. coli* BL21 (DE3) to create the recombinant engineering strain *E. coli* 01. SDS-PAGE results indicated that both enzymes were effectively expressed in *E. coli* 01 (Figure S8). Compounds **14b** and **16b**, which serve as active pharmaceutical scaffolds, were selected for scale preparation under optimized transformation conditions (Figure 6). The whole-cell *E. coli* 01 converted the diketone substrates **14a** and **16a** into bichiral amino alcohols **14b** and **16b**. The diastereomeric ratio (dr) of **14b** (precursor of vernakalant (channel blocker) and anxiolytic medications) was 98:2, with a titer of 6.5 ± 0.05 g L^{-1}. The dr value of **16b** (precursor of ambroxol (mucus dissolving agent) and lomibuvir (hepatitis C protease inhibitor)) was 99:1, with a titer of 12.5 ± 0.15 g L^{-1} (Figure 6 and Figures S28 and S29).

CONCLUSIONS

In conclusion, we developed a substrate-coupled, cofactor-regenerating dual-enzyme cascade system for the one-pot synthesis of high-value bichiral amino alcohols from inexpensive diketones. It is reported for the first time that *Pv*DAPDH can utilize ketone substrates for the asymmetric reductive amination in the synthesis of (*R*)-chiral amines. Furthermore, natural *Bm*GDH was found to have dual functions, in which it not only had the function of cofactor recycling but also reductively hydroxylated ketones to generate chiral alcohols. This work provides a potential biosynthetic pathway for the green production of amino alcohols with multiple chiral centers. However, its catalytic activity still remains low, and it is expected to reform by artificial intelligence to enable the rate-liming enzyme.[32−34]

METHODS

Materials. The expression plasmid pET28a (+) and pRSFDuet-1 and the host strain *E. coli* BL21 (DE3) were purchased from Novagen. Diaminopimelate dehydrogenase (NCBI: WP_075674287.1) was cloned from *Proteus vulgaris*, which was obtained by a prelaboratory screen. L-Amino acid deaminase from *Proteus mirabilis*[35] and glucose dehydrogenase from *Bacillus megaterium* (UniProtKB: A7XZE6_BACME) were preserved by our lab. Commercial reagents, standards, and solvents were purchased from Sigma-Aldrich (Shanghai, China), Meryer Chemicals (Shanghai, China), Aladdin Chemicals (Shanghai, China), Macklin Chemicals (Shanghai, China), and Bide Chemicals (Shanghai, China) and used without further purification.

Expression and Purification of *Pv*DAPDH and GDH. The single colony of recombinant *E. coli* strains *Pv*DAPDH and GDH was cultivated overnight (12−14 h, 37 °C, 180 rpm) in an LB medium containing kanamycin (50 μg mL^{-1}) and used as the inoculum (1%). When the culture's optical density (OD_{600}) reached 0.6−0.8, isopropyl β-D-1-thiogalactopyranoside (IPTG) was added to a final concentration of 0.4 mM to induce gene expression at 25 °C for a further 16 h. The cells were collected by centrifugation (6000*g*, 10 min) and resuspended in buffer A (500 mM NaCl, 20 mM imidazole, 20 mM phosphate buffer, pH 8.5; 10 mL g^{-1} of wet weight). The cell suspensions were lysed by sonication and centrifuged at 14,000*g* for 0.5 h. The subsequent experiments were performed on an ÄKTA pure system (GE Healthcare) with a HisTrap HP column (5 mL, GE Healthcare). The protein was then concentrated for activity assay or catalytic reaction. The purity of proteins was determined by SDS-PAGE. All purification operations were conducted at 4 °C.

Construction, Expression, and Screening of the *Pv*DAPDH Mutation Library. The *Pv*DAPDH mutant libraries of nine amino acid residues including S90, D92, M150, S151, M152, T171, R181, H227, and N253 were generated by applying a saturated mutation with NNK degenerate codons. The mutation libraries were performed with the template plasmid pET28a (+) containing the *Pv*DAPDH gene, and the primers used are listed in Table S3. The colonies were incubated 12 h at 37 °C in 96-well plates containing 200 mL of a fresh lysogeny broth (LB) medium per well. The individual mutants were then transferred to a new 96-deep-well plate (40 mL seed per well containing 800 mL TBA medium) and cultured to an OD_{600} of 0.6 to 0.8, and then the induced cells were cultured overnight at 25 °C. The cell pellets were harvested by centrifugation at 4000*g* for 30 min. The pellets were resuspended in 200 μL of Tris-HCl buffer with 2 mg mL^{-1} lysozyme, and the mixture was then incubated at 37 °C for 2 h with shaking at 400 rpm. The cell-free lysis supernatant was obtained by centrifugation at 4000*g* for 30 min. The reductive amination reaction system (200 μL) consisted of 100 μL of the lysis supernatant, 100 mM NH_4Cl, 10 mM **16c**, and 1.0 mM NADPH in a Tris-HCl buffer (100

https://doi.org/10.1021/acsomega.5c01864
ACS Omega 2025, 10, 23409−23420

mM, pH 8.5). The mixture was reacted in a shaker at 30 °C and 400 rpm for 24 h. To efficiently screen for positive mutants from a 96-well plate, 30 μL of the reaction solution was added to a 96-well plate containing 20 μL of 20 mM 2,4-dinitrophenylhydrazine solution and 70 μL of H_2O. Then the 96-well plates were mixed thoroughly and allowed to react at room temperature for 15 min. Following this, 80 μL of 4 M NaOH solution was added to facilitate color development. After standing in the dark for 15 min, the absorbance of the solution was measured at 520 nm. Next, the combinatorial mutation libraries were obtained via directed evolution methods. All site-directed mutagenesis was performed with the template plasmid pET28a (+) containing the *Pv*DAPDH gene or its mutants, and the primers used are listed in Table S4. All of the mutant libraries were conducted by whole plasmid PCR using KOD-Plus-Neo (TOYOBO). The resultant PCR products were digested with *Dpn*I to eliminate the template plasmid. Furthermore, 10.0 μL of digested products was transformed into *E. coli* BL21(DE3) cells for the following screening or DNA sequencing (GENEWIZ, China).

Construction of the Coexpressed Strain of *Pv*DAPDH and *Bm*GDH. To construct a highly efficient conversion system, coexpression strains were constructed by single enzyme digestion experiments combined with one-step homologous recombination. The main primers used for constructing coexpressed strains are summarized in Table S7. *Pv*DAPDH^{M4} gene was first inserted into pRSFDuet-1 after the first T7 promoter using restriction sites *BamH*I and *Eco*RI. Then *Bm*GDH gene was inserted after the second promoter using the restriction sites *Kpn*I and *Xho*I.

Activity Assays and Kinetic Parameters. The activities of *Pv*DAPDH wild type and its mutant were assayed by measuring the amount of product **16b** that was determined by FDAA derivatization. The activity of GDH was assayed by measuring the initial rate of change in absorbance at 340 nm (corresponding to the amount of NADH (ε = 6220 M^{-1} cm^{-1})) using a microplate reader. One unit (1 U) of activity is defined as the amount of purified enzyme required to produce 1 μM of product. The kinetic parameters of the *Pv*DAPDH wild type and its mutant for reductive amination were determined in a Tris-HCl buffer (100 mM, pH 8.5) at 30 °C, which contained 200 mM NH_4Cl and 5 mM NADPH with various concentrations of **16c** (0−50 mM), and the purified enzyme was added to start the reaction. The kinetic parameter of *Bm*GDH was determined in a Tris-HCl buffer (100 mM, pH 8.5) at 30 °C, which contained 1 mM $NADP^+$, 50 mM D-glucose with various concentrations of **16a** (0−50 mM), and purified *Bm*GDH. All of the experiments were conducted with three replicates. The K_m and k_{cat} values are calculated by fitting the initial rate to the Michaelis−Menten equation with the software Origin.

HPLC Analysis. The concentration and stereoselectivity of amino alcohols were measured with Marfey's reagent (1-fluoro-2,4-dinitrophenyl-5-L-alanine, FDAA) for precolumn derivatization.[22] The mixture consisted of 50 μL of the reaction sample, 100 μL of Marfey's reagent (14 mM) in acetone solution, 80 μL of $NaHCO_3$ (1 M), and 100 μL of ddH_2O. Subsequently, the above mixture was reacted at 80 °C for 10 min. Finally, 40 μL HCl (2 M) was added to stop the reaction. The obtained mixture samples were filtered through a 0.22 μm organic membrane and were then prepared for HPLC analysis. HPLC was performed on an Agilent 1260 system equipped with an Zorbax SB-C18 column (4.6 × 150 mm, 5 μm; Agilent Technologies, USA). The mobile phase was a mixture of ddH_2O (0.1% trifluoroacetic acid; buffer A) and methanol (0.1% trifluoroacetic acid; buffer B). The flow rate was 1.0 mL min^{-1}, the temperature was 25 °C, and detection wavelength was 340 nm. The gradient program was as follows: 40% B, hold for 3 min, increase B to 60% in 4 min, increase B to 80% in 3 min, hold for 3 min, and finally decrease B to 60% in 3 min.

GC Analysis. The reaction samples were repeatedly extracted with an equal volume of ethyl acetate three times, and then the obtained organic phase was dried by anhydrous Na_2SO_4 and filtered through a 0.22 μm organic membrane. The concentration of alcohol products was detected using GC. GC was performed on a SHIMADZU Nexis GC-2030AF system, which is equipped with a DB-5 chromatographic column (30 m × 0.25 mm × 0.25 μm; Agilent Technologies, Inc.) and nitrogen as the carrier gas. GC conditions were as follows: carrier gas flow rate: 1.0 mL min^{-1}, split ratio: 10:1, injector temperature: 250 °C, and FID detector: 270 °C. The temperature program was as follows: the initial column temperature was set at 60 °C and hold for 1 min; then increased at 10 °C min^{-1} up to 90 °C; finally, increased at 20 °C min^{-1} up to 250 °C , maintained for 2 min.

The concentration and stereoselectivity of alcohol products were detected using chiral GC. Chiral GC was performed on a SHIMADZU Nexis GC-2030AF system, which is equipped with a CP-Chiralsil-Dex CB chromatographic column (25 m × 0.25 mm × 0.25 μm; Agilent Technologies, Inc.) and nitrogen as the carrier gas.[36] Chiral GC conditions were as follows: injector: 250 °C, FID detector: 270 °C, carrier gas flow rate: 1.0 mL min^{-1}, and split ratio: 10:1. The temperature program was as follows: the initial column temperature was set at 80 °C; then increased at 20 °C min^{-1} up to 100 °C; next, increased at 10 °C min^{-1} up to 130 °C hold for 1 min, then increased at 5 °C min^{-1} up to 160 °C hold for 1 min;finally, increased at 5 °C min^{-1} up to 200 °C, maintained for 2 min.

Molecular Docking. Using the *Pv*DAPDH-NADPH binary complex as a model, **16c** and NH_4^+ were docked to the active center, and then the dynamically stable *Pv*DAPDH-**16c**_NH_4^+_NADPH complex structures were obtained through MD simulation. Similarly, **16c**_Int2 was docked to the active center of the *Pv*DAPDH-NADPH binary complex, and then the dynamically stable *Pv*DAPDH-**16c**_Int2-NADPH complex structure was obtained through MD simulation. Next, the starting structure coordinates of mutant M4 were created by changing multiple mutated residues. Then, substrate **16c** and intermediate **16c**_Int2 were docked into the active center of mutant M4 using AutoDock Vina followed by MD simulations.[37] The docking parameters used for the molecular docking of the ligand into the active site of *Pv*DAPDH via AutoDock Vina were as follows: The grid box was centered on the active site of *Pv*DAPDH with dimensions of 30 × 30 × 30 Å to ensure sufficient coverage of the binding pocket, and the exhaustiveness parameter was set to 8 to balance computational efficiency and docking accuracy. The top 20 docking poses were generated and analyzed using the default scoring function of AutoDock Vina.

Molecular Dynamic Simulations. The substrate-bound complex conformation was selected for the molecular dynamics (MD) simulation. The titratable residues (His, Glu, Asp, Lys, and Arg) were assigned based on their pK_a data derived from the PROPKA program.[38] Moreover, the protonation states and local hydrogen bond networks were

https://doi.org/10.1021/acsomega.5c01864
ACS Omega 2025, 10, 23409−23420

further carefully checked using the VMD software.[39] Histidine residues His111, His179, His241, and His227 were set as HID, while His94, His154, His212, His230, and His233 were set as HIE. All glutamic acid and aspartic acid residues were deprotonated. All of the lysine and arginine residues were protonated. For the further MD simulations, the typical AMBER force field (GAFF)[40] was implemented for the ligands, whereas the partial atomic charges were received from the RESP method[41] utilizing the B3LYP-D3/6-31G (d, p) level of theory. The Amber ff14SB force field[42] was used for protein residues. Each simulation system was solvated in a rectangular box filled with TIP3P water and neutralized by Na^+ counterions. Next, each system was equilibrated with a series of minimizations interspersed by short MD simulations during which restraints on the protein backbone heavy atoms were gradually released (with a force constant of 10, 2, 0.1, and 0 kcal/(mol·Å^2)) and heated slowly from 0 to 310 K for 50 ps in which we applied a 10 kcal/(mol·Å^2) restraint on the protein backbone heavy atoms. Finally, an extensive MD simulation of 100 ns was performed at a constant temperature and pressure. All MD simulations were performed using the Amber 18 package.[43]

■ ASSOCIATED CONTENT

Supporting Information

The Supporting Information is available free of charge at https://pubs.acs.org/doi/10.1021/acsomega.5c01864.

DNA sequence, amino acid sequence, and functional verification of the *Bm*GDH/*Pv*DAPDH data; mutant primers; mutation library screening data; substrate scope determination data; kinetic parameter data; SDS-PAGE; construction of gene coexpression plasmid; substrate concentration ratio optimization data; and HPLC, GC, and MS analysis data of the production (PDF)

■ AUTHOR INFORMATION

Corresponding Authors

Wanqing Wei − *School of Biotechnology and Key Laboratory of Industrial Biotechnology of Ministry of Education, Jiangnan University, Wuxi 214122, China*; Phone: +86-510-85910057; Email: wanqwei@163.com

Liming Liu − *School of Biotechnology and Key Laboratory of Industrial Biotechnology of Ministry of Education, Jiangnan University, Wuxi 214122, China*; Phone: +86-510-85197875; Email: mingll@jiangnan.edu.cn

Authors

Tianfu Wu − *School of Biotechnology and Key Laboratory of Industrial Biotechnology of Ministry of Education and School of Life Sciences and Health Engineering, Jiangnan University, Wuxi 214122, China*; orcid.org/0000-0001-7401-3267

Wei Song − *School of Life Sciences and Health Engineering, Jiangnan University, Wuxi 214122, China*; orcid.org/0000-0002-2278-2205

Jing Wu − *School of Biotechnology and Key Laboratory of Industrial Biotechnology of Ministry of Education and School of Life Sciences and Health Engineering, Jiangnan University, Wuxi 214122, China*

Jian Wen − *School of Life Sciences and Health Engineering, Jiangnan University, Wuxi 214122, China*; orcid.org/0000-0002-7285-0923

Complete contact information is available at: https://pubs.acs.org/10.1021/acsomega.5c01864

Author Contributions

T.W. and L.L. designed this project. T.W. performed this project. J.W., J.W., and W.S. analyzed this project. T.W. and W.W. wrote this manuscript.

Notes

The authors declare no competing financial interest.

■ ACKNOWLEDGMENTS

This work was supported by the Science Fund for Creative Research Groups of the National Natural Science Foundation of China (32021005), the Youth Program of National Natural Science Foundation of China (22407051), and the General Program of National Natural Science Foundation of China (22378165).

■ REFERENCES

(1) Chamberlain, P. D.; Sadaka, A.; Berry, S.; Lee, A. G. Ethambutol optic neuropathy. *Curr. Opin. Ophthalmol.* **2017**, *28* (6), 545−551.

(2) Pan, S.; Jiang, M.; Hu, J.; Xu, R.; Zeng, X.; Zhong, G. Synthesis of 1,2-amino alcohols by decarboxylative coupling of amino acid derived α-amino radicals to carbonyl compounds via visible-light photocatalyst in water. *Green Chem.* **2020**, *22* (2), 336−341.

(3) Sun, J.; Wang, S.; Harper, K. C.; Kawamata, Y.; Baran, P. S. Stereoselective amino alcohol synthesis via chemoselective electrocatalytic radical cross-couplings. *Nat. Chem.* **2025**, 44.

(4) Nakafuku, K. M.; Zhang, Z.; Wappes, E. A.; Stateman, L. M.; Chen, A. D.; Nagib, D. A. Enantioselective radical C−H amination for the synthesis of β-amino alcohols. *Nat. Chem.* **2020**, *12* (8), 697−704.

(5) Elfadil, A.; Alzahrani, A. M.; Abdullah, H.; Alsamhan, H.; Abujamel, T. S.; Ahmed, H. E.; Jiman-Fatani, A. Evaluation of the antibacterial activity of quinoxaline derivative compound against methicillin-resistant staphylococcus aureus. *Infect. Drug Resist.* **2023**, *16*, 2291−2296.

(6) Nilov, D.; Reiser, O. The sharpless asymmetric amino-hydroxylation scope and limitation. *Adv. Synth. Catal.* **2002**, *344* (10), 1169−1173.

(7) Adderley, N. J.; Buchanan, D. J.; Dixon, D. J.; Lainé, D. I. Highly diastereoselective oxy-michael additions of enantiopure δ-lactol anions to nitroalkenes: asymmetric synthesis of 1,2-amino alcohols. *Angew. Chem., Int. Ed.* **2003**, *42* (35), 4241−4244.

(8) Hu, Q.; Chen, J.; Zhang, Z.; Liu, Y.; Zhang, W. Rh-catalyzed one-pot sequential ssymmetric hydrogenation of α-dehydroamino ketones for the synthesis of chiral cyclic trans-β-amino alcohols. *Org. Lett.* **2016**, *18* (6), 1290−1293.

(9) Wang, J.; Lin, X.; Shao, P.-L.; Song, J.; Wen, J.; Zhang, X. Double asymmetric hydrogenation of α-Iminoketones: facile synthesis of enantiopure vicinal amino alcohols. *ACS Catal.* **2021**, *11* (20), 12729−12735.

(10) Karjalainen, O. K.; Koskinen, A. M. P. Diastereoselective synthesis of vicinal amino alcohols. *Org. Biomol. Chem.* **2012**, *10* (22), 4311.

(11) Fan, G.; Liu, Y. Titanium-mediated cross-coupling reactions of imines with ketones or aldehydes: an efficient route for the synthesis of 1,2-amino alcohols. *Tetrahedron Lett.* **2012**, *53* (38), 5084−5087.

(12) Liu, S.; Xie, J.-H.; Li, W.; Kong, W.-L.; Wang, L.-X.; Zhou, Q.-L. Highly enantioselective synthesis of chiral cyclic amino alcohols and conhydrine by Ruthenium-catalyzed asymmetric hydrogenation. *Org. Lett.* **2009**, *11* (21), 4994−4997.

(13) Birrell, J. A.; Jacobsen, E. N. A practical method for the synthesis of highly enantioenriched trans-1, 2-amino alcohols. *Org. Lett.* **2013**, *15* (12), 2895−2897.

(14) Yang, Z.-P.; Freas, D. J.; Fu, G. C. The asymmetric synthesis of amines via Nickel-catalyzed enantioconvergent substitution reactions. *J. Am. Chem. Soc.* **2021**, *143* (7), 2930−2937.

(15) Leone, M.; Milton, J. P.; Gryko, D.; Neuville, L.; Masson, G. TBADT-mediated photocatalytic stereoselective radical alkylation of chiral N-sulfinyl imines: towards efficient synthesis of diverse chiral amines. *Chem. - Eur. J.* **2024**, *30* (24), 1−6.
(16) Ye, C. X.; Melcamu, Y. Y.; Li, H. H.; Cheng, J. T.; Zhang, T. T.; Ruan, Y. P.; Zheng, X.; Lu, X.; Huang, P. Q. Dual catalysis for enantioselective convergent synthesis of enantiopure vicinal amino alcohols. *Nat. Commun.* **2018**, *9* (1), 410−418.
(17) Pavlidis, I. V.; Weiß, M. S.; Genz, M.; Spurr, P.; Hanlon, S. P.; Wirz, B.; Iding, H.; Bornscheuer, U. T. Identification of (*S*)-selective transaminases for the asymmetric synthesis of bulky chiral amines. *Nat. Chem.* **2016**, *8* (11), 1076−1082.
(18) Zhang, J.-D.; Zhao, J.-W.; Gao, L.-L.; Chang, H.-H.; Wei, W.-L.; Xu, J.-H. Enantioselective synthesis of enantiopure *β*-amino alcohols via kinetic resolution and asymmetric reductive amination by a robust transaminase from *Mycobacterium vanbaalenii*. *J. Biotechnol.* **2019**, *290*, 24−32.
(19) Chen, F.-F.; Cosgrove, S. C.; Birmingham, W. R.; Mangas-Sanchez, J.; Citoler, J.; Thompson, M. P.; Zheng, G.-W.; Xu, J.-H.; Turner, N. J. Enantioselective synthesis of chiral vicinal amino alcohols using amine dehydrogenases. *ACS Catal.* **2019**, *9* (12), 11813−11818.
(20) Wang, H.; Qu, G.; Li, J.-K.; Ma, J.-A.; Guo, J.; Miao, Y.; Sun, Z. Data mining of amine dehydrogenases for the synthesis of enantiopure amino alcohols. *Catal. Sci. Technol.* **2020**, *10* (17), 5945−5952.
(21) Liu, L.; Wang, D. H.; Chen, F. F.; Zhang, Z. J.; Chen, Q.; Xu, J. H.; Wang, Z. L.; Zheng, G. W. Development of an engineered thermostable amine dehydrogenase for the synthesis of structurally diverse chiral amines. *Catal. Sci. Technol.* **2020**, *10* (8), 2353−2358.
(22) Ming, H.; Yuan, B.; Qu, G.; Sun, Z. Engineering the activity of amine dehydrogenase in the asymmetric reductive amination of hydroxyl ketones. *Catal. Sci. Technol.* **2022**, *12* (19), 5952−5960.
(23) Li, Y.; Hu, N.; Xu, Z.; Cui, Y.; Feng, J.; Yao, P.; Wu, Q.; Zhu, D.; Ma, Y. Asymmetric synthesis of N-substituted 1,2-amino alcohols from simple aldehydes and amines by one-pot sequential enzymatic hydroxymethylation and asymmetric reductive amination. *Angew. Chem., Int. Ed.* **2022**, *61* (17), No. e202116344.
(24) Mayol, O.; Bastard, K.; Beloti, L.; Frese, A.; Turkenburg, J. P.; Petit, J.-L.; Mariage, A.; Debard, A.; Pellouin, V.; Perret, A.; de Berardinis, V.; Zaparucha, A.; Grogan, G.; Vergne-Vaxelaire, C. A family of native amine dehydrogenases for the asymmetric reductive amination of ketones. *Nat. Catal.* **2019**, *2* (4), 324−333.
(25) Cao, J.; Hyster, T. K. Pyridoxal-catalyzed racemization of *α*-aminoketones enables the stereodivergent synthesis of 1,2-amino alcohols using ketoreductases. *ACS Catal.* **2020**, *10* (11), 6171−6175.
(26) Liu, Y.; Zhu, L.; Li, X.; Cui, Y.; Roosta, A.; Feng, J.; Chen, X.; Yao, P.; Wu, Q.; Zhu, D. Photoredox/enzymatic catalysis enabling redox-neutral decarboxylative asymmetric C−C coupling for asymmetric synthesis of chiral 1,2-amino alcohols. *JACS Au* **2023**, *3* (11), 3005−3013.
(27) Cho, I.; Prier, C. K.; Jia, Z. J.; Zhang, R. K.; Görbe, T.; Arnold, F. H. Enantioselective aminohydroxylation of styrenyl olefins catalyzed by an engineered hemoprotein. *Angew. Chem., Int. Ed.* **2019**, *58* (10), 3138−3142.
(28) Sviatenko, O.; Ríos-Lombardía, N.; Morís, F.; González-Sabín, J.; Venkata Manideep, K.; Merdivan, S.; Günther, S.; Süss, P.; Höhne, M. One-pot synthesis of 4-aminocyclohexanol isomers by combining a keto reductase and an amine transaminase. *ChemCatChem.* **2019**, *11* (23), 5794−5799.
(29) Aleku, G. A.; France, S. P.; Man, H.; Mangas-Sanchez, J.; Montgomery, S. L.; Sharma, M.; Leipold, F.; Hussain, S.; Grogan, G.; Turner, N. J. A reductive aminase from *Aspergillus oryzae*. *Nat. Chem.* **2017**, *9* (10), 961−969.
(30) Gao, X.; Zhang, Z.; Zhang, Y.; Li, Y.; Zhu, H.; Wang, S.; Li, C.; Atomi, H. A newly determined member of the *meso*-diaminopimelate dehydrogenase family with a broad substrate spectrum. *Appl. Environ. Microbiol.* **2017**, *83* (11), No. e00476.
(31) Wu, T.; Chen, Y.; Wei, W.; Song, W.; Wu, J.; Wen, J.; Hu, G.; Li, X.; Gao, C.; Chen, X.; Liu, L. Mechanism-guided computational design drives *meso*-diaminopimelate dehydrogenase to efficient synthesis of aromatic D-amino acids. *ACS Synth. Biol.* **2024**, *13* (6), 1879−1892.
(32) Yang, K. K.; Wu, Z.; Arnold, F. H. Machine-learning-guided directed evolution for protein engineering. *Nat. Methods* **2019**, *16* (8), 687−694.
(33) Eisenstein, M. AI-enhanced protein design makes proteins that have never existed. *Nat. Biotechnol.* **2023**, *41* (3), 303−305.
(34) Jiang, K.; Yan, Z.; Di Bernardo, M.; Sgrizzi, S. R.; Villiger, L.; Kayabolen, A.; Kim, B. J.; Carscadden, J. K.; Hiraizumi, M.; Nishimasu, H.; Gootenberg, J. S.; Abudayyeh, O. O. Rapid in silico directed evolution by a protein language model with EVOLVEpro. *Science* **2025**, 1−21.
(35) Wu, Y.; Zhang, S.; Song, W.; Liu, J.; Chen, X.; Hu, G.; Zhou, Y.; Liu, L.; Wu, J. Enhanced catalytic efficiency of L-amino acid deaminase achieved by a shorter hydride transfer distance. *ChemCatChem.* **2021**, *13* (21), 4557−4566.
(36) Zhang, J.; Dong, R.; Yang, X.; Gao, L.; Zhang, C.; Ren, F.; Li, J.; Chang, H. Characterization of four diol dehydrogenases for enantioselective synthesis of chiral vicinal diols. *Chin. J. Chem. Eng.* **2022**, *47*, 145−154.
(37) Tang, S.; Chen, R.; Lin, M.; Lin, Q.; Zhu, Y.; Ding, J.; Hu, H.; Ling, M.; Wu, J. Accelerating autodock vina with GPUs. *Molecules* **2022**, *27* (9), 3041−3059.
(38) Olsson, M. H. M.; Søndergaard, C. R.; Rostkowski, M.; Jensen, J. H. Propka3: consistent treatment-of internal and surface residues in empirical pka predictions. *J. Chem. Theory Comput.* **2011**, *7* (2), 525−537.
(39) Humphrey, W.; Dalke, A.; Schulten, K. VMD: visual molecular dynamics. *J. Mol. Graph* **1996**, *14* (1), 33−38.
(40) Wang, J.; Wolf, R. M.; Caldwell, J. W.; Kollman, P. A.; Case, D. A. Development and testing of a general amber force field. *J. Comput. Chem.* **2004**, *25* (9), 1157−1174.
(41) Bayly, C. I.; Cieplak, P.; Cornell, W.; Kollman, P. A. A well-behaved electrostatic potential based method using charge restraints for deriving atomic charges: the RESP model. *J. Phys. Chem.* **1993**, *97* (40), 10269−10280.
(42) Maier, J. A.; Martinez, C.; Kasavajhala, K.; Wickstrom, L.; Hauser, K. E.; Simmerling, C. ff14SB: Improving the accuracy of protein side chain and backbone parameters from ff99SB. *J. Chem. Theory Comput.* **2015**, *11* (8), 3696−3713.
(43) Frisch, M. J.; Trucks, G. W.; Schlegel, H. B.; Scuseria, G. E.; Robb, M. A.; Cheeseman, J. R.; Scalmani, G.; Barone, V.; Petersson, G. A.; Nakatsuji, H. L. X.; Caricato, M. M. A. V.; Bloino, J.; Janesko, B. G.; Gomperts, R.; Mennucci, B.; Hratchian, H. P.; Ortiz, J. V.; Izmaylov, A. F.; Sonnenberg, J. L.; Williams; Ding, F.; Lipparini, F.; Egidi, F.; Goings, J.; Peng, B.; Petrone, A.; Henderson, T.; Ranasinghe, D.; Zakrzewski, V. G.; Gao, J.; Rega, N.; Zheng, G.; Liang, W.; Hada, M.; Ehara, M.; Toyota, K.; Fukuda, R.; Hasegawa, J.; Ishida, M.; Nakajima, T.; Honda, Y.; Kitao, O.; Nakai, H.; Vreven, T.; Throssell, K.; Montgomery, Jr., J. A.; Peralta, J. E.; Ogliaro, F.; Bearpark, M. J.; Heyd, J. J.; Brothers, E. N.; Kudin, K. N.; Staroverov, V. N.; Keith, T. A.; Kobayashi, R.; Normand, J.; Raghavachari, K.; Rendell, A. P.; Burant, J. C.; Iyengar, S. S.; Tomasi, J.; Cossi, M.; Millam, J. M.; Klene, M.; Adamo, C.; Cammi, R.; Ochterski, J. W.; Martin, R. L.; Morokuma, K.; Farkas, O.; Foresman, J. B.; Fox, D. J. *Amber 2018*. University of California: San Francisco, 2018.

https://doi.org/10.1021/acsomega.5c01864
ACS Omega 2025, 10, 23409−23420